Stabilizing *p*-type conductivity in CuYO$_2$ by co-doping: A first-principles study

T. Premkumar [a], R. Vidya [a,*], Helmer Fjellvåg [b]

[a] *Computational Laboratory for Multi-functional Materials, Department of Medical Physics, College of Engineering, Anna University, Sardar Patel Road, Guindy, 600025, India*
[b] *Centre for Materials Science and Nanotechnology, Department of Chemistry, University of Oslo, Box 1033, Blindern, N-0315, Oslo, Norway*

HIGHLIGHTS

- Chemical potential based stability diagram for CuYO$_2$.
- Oxygen interstitial is shown to stabilize the defect complexes.
- *p*-type conductivity is enhanced by co-doping of B$_Y$ together with O$_i$.
- Mapping the inter band transitions with the peaks in the optical spectra.

ARTICLE INFO

ABSTRACT

This work figures out the importance of *p*-type conductive materials through first-principle calculations. It is shown that the co-doping mechanism can enhance the *p*-type conductivity of CuYO$_2$. Substituting Boron at the Yttrium (B$_Y$) site, together with Oxygen at interstitial positions (O$_i$), introduces shallow acceptor levels just above the valence band maximum (VBM). From the thermodynamical calculations, the stability of defects was also confirmed in O-rich synthesis conditions. A detailed analysis of the electronic band structure shows that the VBM and CBM can be tuned by introducing suitable impurities. Likewise, the substitutional impurities Ge and In at Y sites (Ga$_Y$ and In$_Y$) are shown to have high electronic conductivity. We have demonstrated the possibility of ambipolar charge carriers in CuYO$_2$ by co-doping.

1. Introduction

The modern electronic industry needs high-performance optoelectronic devices with better efficiency to cope with the future energy challenge. Indeed, the efficiency of such devices relies on the properties of constituent semiconductor materials. Researchers have received considerable attention in transparent conducting oxide (TCO) materials in recent decades due to their underlying physical properties like wide-bandgap nature and good electrical conductivity. Moreover, they have a wide range of technological applications such as transparent contact in flat panel displays, light-emitting diodes, optical sensors [1,2], photovoltaic devices [3], and low emissivity windows [4], etc. Although many *n*-type TCOs such as Tin Oxide (SnO$_2$) [5], Indium Oxide (In$_2$O$_3$) [6], Tin doped Indium Oxide (ITO) [7], and ZnO [8] have been discovered and widely used in optoelectronic applications, a dearth in their *p*-type

counterparts impede the advancements of transparent *p*−*n* junction formation to develop the next generation high-efficiency electronic devices called invisible electronics [9]. In this aspect, exploring new materials with enhanced *p*-type conductivity is an immense challenge.

Copper-based delafossite materials of type Cu*M*O$_2$ (*M* = B, Al, In, Ge, Fe, Cr, Sc, and Y [10–20]) are having wide bandgap (greater than 3.1 eV) nature and also natural *p*-type conductivity. These materials started to attract the attention of researchers when Kawazoe et al. [13], first reported naturally occurring *p*-type conductivity with good transparency in the polycrystalline thin films of CuAlO$_2$ prepared using laser ablation method [13]. Thus prepared CuAlO$_2$ showed a bandgap (E$_g$) of 3.5 eV from the optical absorption measurements, and the maximum obtained Hall mobility of positive holes was 10.4 cm^{2}V^{-1}s^{-1} [13]. Even though the obtained Hall mobility of holes in CuAlO$_2$ is comparable to that of ITO, it is less than the conductivity of conventional *n*-type TCOs. All

---

* Corresponding author.
E-mail addresses: prem.unom@gmail.com (T. Premkumar), vidyar@annauni.edu (R. Vidya).

other delafossite materials with different trivalent cations also exhibit small *p*-type conductivity, which must be improved to use them efficiently. Efforts have been made to improve the *p*-type conductivity in delafossite structured materials by creating suitable defects. However, increasing the conductivity of holes by suitable doping leads to a decrease in transparency and vice versa. Hence, many research efforts are needed to enhance the conductivity of *p*-type TCOs without compromising their transparency.

Generally, the electrical conductivity of copper-based delafossite compounds is increased by suitable doping and also depends on the size of trivalent cations [14]. Furthermore, the electrical conductivity is directional dependant [20,21], and for hole conductivity, these materials adopt a small polaron hopping mechanism [22]. Among the copper delafossite compounds with trivalent cations of group IIIB elements (such as B, Al, Ga, and In), $CuGaO_2$ shows the highest conductivity of 1 S cm^{-1} by Fe substitution instead of Ga [18]. Both $CuAlO_2$ and $CuInO_2$ show improved *p*-type conductivity by N (at interstitial site) [23] and Ca (instead of In) [19] doping, respectively, which is less than that of $CuGaO_2$, besides $CuInO_2$ shows *n*-type conductivity with Sn doping [19]. Moreover, Oxygen interstitial in delafossite compounds also increases the hole concentration and *p*-type conductivity. However, doping Oxygen at interstitial sites needs large trivalent cations [15]. Hence, compounds with trivalent cations of group IIIA elements (such as Sc, Y, and La) are more favourable to the Oxygen intercalation. It is observed that, $CuScO_2$ can be oxidized up to $CuScO_{2.5}$ [15], $CuYO_2$ and $CuLaO_2$ can be oxidized up to $CuYO_{2.55}$ and $CuLaO_{2.64}$ [11], respectively. The oxidized $CuScO_2$ thin films show more *p*-type conductivity (30 Scm^{-1}) [12] compared to that of $CuScO_2$ thin films with 5% Mg doping (2.28 Scm^{-1}) [15], but the transparency is reduced to 40% in the visible region. However, the Oxygen intercalation in Ca doped $CuYO_2$ showed larger *p*-type conductivity (8 S cm^{-1}) than that of other defects in $CuYO_2$. However, with a simultaneous decrease in the transparency from 60% to 45% in the visible region [24]. All available results revealed that the *p*-type conductivity of delafossite compounds increased by suitable doping, but this correspondingly reduces the transparency [12,15,24] and vice versa [25].

Many theoretical reports were available on copper-based delafossite compounds, which underestimate the band gaps due to the poor description of exchange-correlation effects between the electrons. Among them, the Hartree-Fock method predicts considerable covalent character in O–Cu–O fragments and strong ionic nature of bonding between trivalent cations and Oxygen [26]. Furthermore, band structure calculations using Full-Potential Linear Muffin-Tin Orbitals (FPLMTO) method with local density approximation (LDA) estimates the bandgap of 1.95 eV [27] for $CuAlO_2$ and 3.3 eV for $CuYO_2$ [28], whereas the generalized-gradient approximation (GGA) using projected augmented wave (PAW) pseudopotential predicts the indirect bandgap of 0.49 eV [16] for $CuInO_2$ and 2.62 eV for $CuYO_2$ [29]. In addition to that, the possibility of bipolar doping in $CuMO_2$ (M = Sc, Y) was also explored by the first-principle calculations using PAW pseudo potential within LDA [30]. The defect calculation using PAW with LDA as an exchange-correlation functional reported that the vacancy of Cu and Oxygen interstitial is the most efficient acceptors [31] in these compounds. $CuYO_2$ can easily host Oxygen interstitial compared to other delafossite compounds because of its large Cu–Cu distance [32]. Moreover, calcium dopant [33,34] and oxygen interstitial [11,24] in $CuYO_2$ enhances the *p*-type conductivity than the undoped one and other $CuXO_2$ (X = B, Al, Ga and In) delafossite compounds. Moreover, the cost of Y is less than that of Sc, so that $CuYO_2$ might become a promising optoelectronic material in the future.

Similar to other delafossites, the transparency of $CuYO_2$ decreases while increasing the Ca or Oxygen dopant concentration and vice versa. Hitherto, no theoretical study is available to explain the effects of different substitutional and interstitial doping in $CuYO_2$. Also, no report shows an increase in both conductivity and transparency simultaneously. In this work, we attempt to study the effect of various defects

such as interstitial Oxygen (O_i), Yttrium vacancy ($Y_\square$), Yttrium substituted by B, Al, Ga and In (B_Y, Al_Y, Ga_Y, and In_Y) and defect complexes (Yttrium substituents together with Oxygen interstitial) in the supercell of $CuYO_2$. Electronic band structure, the density of states (DOS), effective mass, charge density, electron localization function (ELF), and optical properties are calculated and analyzed in detail.

2. Computational details

Vienna *ab-initio* simulation package (VASP) [35] based on projected augmented plane wave method [36] was used to explore the material properties. The kinetic energy cut-off of 500 eV was considered for structural optimization, and 400 eV was used for electronic structure and optical properties calculations. The ions are completely optimized by minimizing the force and stress with convergence criteria of 10^{-6} eV per unit cell and ≤ 1 meVÅ^{-1} for total energy and force, respectively. The exchange-correlation interaction between the electrons treated as GGA [37] with PBE functional throughout the calculations. Owing to the supercell calculations of pristine and various defects, a gamma-centered k-points grid of $8 \times 8 \times 4$ and $4 \times 4 \times 2$ with Monkhorst-Pack [38] scheme was used for structural optimization and materials properties calculations, respectively. The accurate band gap of pristine $CuYO_2$ supercell was calculated with screened hybrid functional as proposed by Heyd, Scuseria, and Ernzerhof (HSE06 [39]) with crystalline structure optimized using GGA. Vesta 3D visualization tool [40] was used to plot Crystal structure, polyhedral type, charge density, and ELF.

Since this work emphasizes the study of charged point defects, correcting the defect formation energy is needed to avoid the interaction between the defects and their periodic images. Herein, the Freysoldt-Neugebauer-Van de Walle (FNV) correction scheme [41] implemented in the CoFFEE package [42].

3. Results and discussion

3.1. Structural investigations

Experimentally $CuYO_2$ crystallizes in rhombohedral and hexagonal symmetry structures described with space group of $R-3m$ (166) [43] and $P6_3/mmc$ (194) [44], respectively. These experimental structural parameters are optimized completely by the above-said criteria and found that the optimized structural parameters were in good agreement with the experimental parameters. There are 0.4% and 0.5% variations in the optimized lattice parameters and the angle, respectively, from the experimental values for the rhombohedral structure. In the hexagonal structure, the variations of optimized lattice parameters *a* and *c* from the experimental values were obtained as 1.2% and 0.4%, respectively. Due to extra coupling between the occupied O *p* and unoccupied Y *d* electronic states in hexagonal symmetry [29], the calculated formation energy is 3 meV/fu lower than that of the rhombohedral structure. As the energy difference between rhombohedral and hexagonal structures is negligible, the experimentally synthesized $CuYO_2$ may have the possibility to exhibit mixing both of these phases, depending on the growth conditions. We have considered the hexagonal structure for calculating the physical properties. In this structure, the Cu atoms are linearly coordinated with O, and Y atoms are octahedrally coordinated with O. The O–Cu–O linear chain connects the YO_6 octahedra and builds the complete structure.

3.2. Phase diagram of $CuYO_2$ from chemical potential

The formation of native defects in $CuYO_2$ is subject to the chemical potential reservoirs in their elemental phases. The individual chemical potentials (μ_x) of isolated atoms are not equal to their stable elemental form. Hence, it can be written as $\mu_x = \mu_x^{solid}/gasgas + \Delta\mu_x$, where $\Delta\mu_x$ are the varying chemical potential for the respective element. Under

thermodynamical equilibrium, the formation energy must follow [45].

$$\Delta H_f(CuYO_2) = \Delta\mu_{Cu} + \Delta\mu_Y + 2\Delta\mu_O \qquad (1)$$

Moreover, $\Delta\mu_{Cu} < 0$, $\Delta\mu_Y < 0$, and $\Delta\mu_O < 0$. Herein, the metal-rich and Oxygen-rich are corresponding to $\Delta\mu_{Cu/Y} = 0$ and $\Delta\mu_O = 0$, respectively. Furthermore, to extract the stability phase of $CuYO_2$, the formation of competing binary phases is also considered. For example Y_2O_3 and CuO are the binaries of $CuYO_2$, then the following constraint equations $2\Delta\mu_Y + 3\Delta\mu_O \leq \Delta H_f(Y_2O_3)$ and $\Delta\mu_{Cu} + \Delta\mu_O \leq \Delta H_f(CuO)$, respectively, must be accounted to confirm the stability of $CuYO_2$. Therefore, all considered binaries and their formation energies are listed in table ST1 in the supplementary material. The thermodynamic stability of $CuYO_2$ is accounted by considering the formation energies of these binaries. The total energy from the optimized FCC phase of Cu and trigonal phase of Y and their respective total energy was taken as their stable elemental chemical potential. Besides, the total energy of isolated and optimized O_2 dimer in a 15 Å cubic cell was used to fix the stable elemental chemical potential of Oxygen $(E(O) = \frac{1}{2}E(O_2))$. By considering all of the above-said constraints as well as the constraint equations of considered competing binaries listed, the chemical potential-based stability diagram was constructed (see Fig. 1) for $CuYO_2$.

The stability of $CuYO_2$ is governed by the region enclosed with the points ABCDEFGA. Each stability point represents the change in elements' respective atomic chemical potentials. Further, lines parallel to the $\mu_O = 0$ represent the same $\Delta\mu_O$ and the point where $\Delta\mu_{Cu}$ and $\Delta\mu_Y$ are zero is taken as Oxygen poor condition $(\Delta\mu_O = -4.86)$. The defect formation energies of considered defects are evaluated in these different chemical potential varying conditions.

3.3. Modelling defects

The supercells constructed with 32 and 144 atoms by extending the lattice parameters of the unit cell as $2 \times 2 \times 1$ and $3 \times 3 \times 2$, respectively, were considered for the defect calculations. The calculated formation energy for 32 atom supercell is 0.4 meV/fu, more than that of 144 atom supercell. The slight difference in this energy could not make any significant deviation in the results. Moreover, calculations with 32 atom supercells are computationally less expensive. Hence, the 32 atom supercell (a = 7.1347 Å, c = 11.4633 Å) was considered for the defect calculations. The supercells with defects like interstitial Oxygen (O_i), Yttrium vacancy $(Y_\square)$, B, Al, Ga and In substituted for Y (B_Y, Al_Y, Ga_Y, In_Y), and substitutions with Oxygen interstitial $(B_Y + O_i, Al_Y + O_i, Ga_Y + O_i, and In_Y + O_i)$ were modelled, and their structural parameters are optimized with the above-said criteria.

The interstitial Oxygen atom initially taking the linear position with Cu atoms along the b-axis (Fig. 2(a)) is displaced to the centroid of a triangle (Fig. 2(b)) constructed by three Cu atoms after complete structural relaxation. Further, it shows that the Oxygen moves only on the plane of the Cu atoms (see Fig. 2(c) and (d)), as pointed out in the experimental works [38, 5]. But, the octahedral coordination of Y situated above and below the O_i is distorted due to insufficient electron gain from the surrounding Cu atoms. Other defects such as the substitution of B, Al, Ga, and In instead of Y (see Fig. S1(a)) also slightly affect the O–Cu–O linear chain (see Fig. S1(b)).

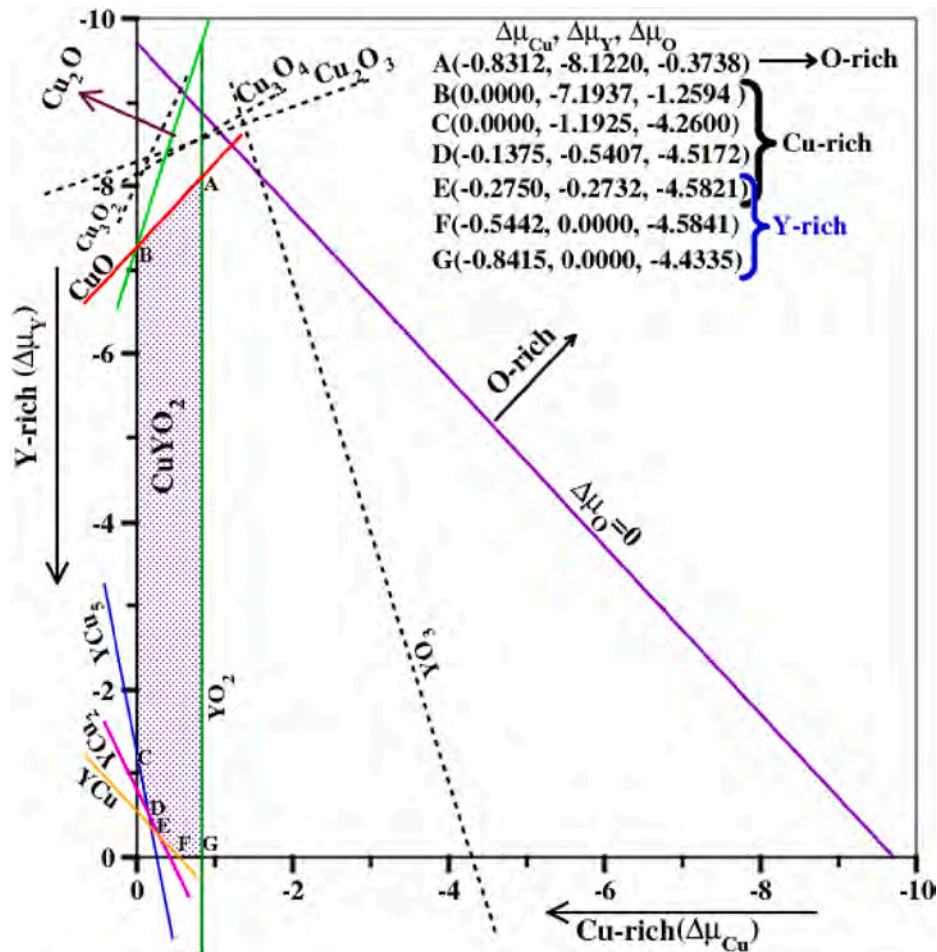The optimized interatomic distances between the constituent atoms

Fig. 1. Phase stability diagram of $CuYO_2$, the region enclosed by the points ABCDEFG represents the stability region of $CuYO_2$. Lines inside the diagram are corresponding to the constraint equation of respective binary compounds. Here, the chemical potentials are in the unit of eV.
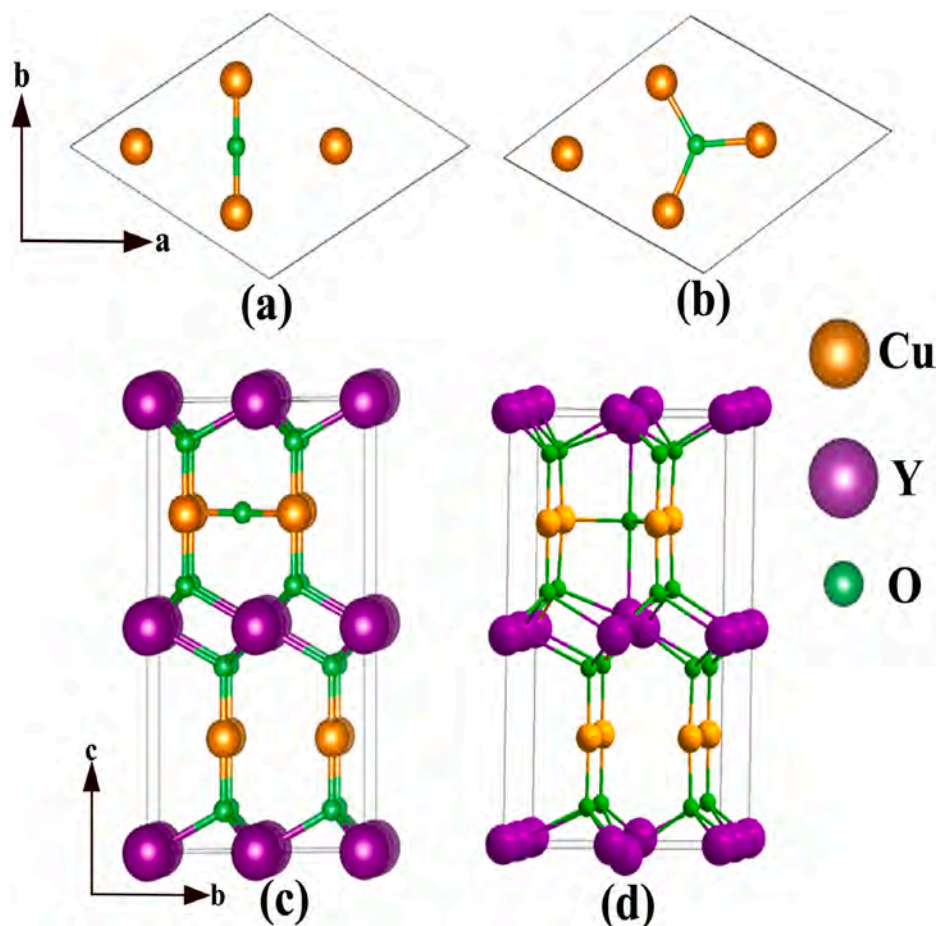
Fig. 2. Delafossite structure (Hexagonal phase) of CuYO$_2$ with Oxygen interstitial, projected along c-axis (a.) Initial. (b.) Projected along the a-axis (c.)Initial (d.) Optimized.

in the defect complexes are (see Table 1) compared with that of the pristine supercell. The optimized interatomic distances between the constituent atoms in the pristine supercell are in good agreement with the available theoretically calculated values using LDA [46,47] and GGA [48] functional and also with experimentally observed values [43]. In the defect Y$_\square$, the Oxygen atoms close to Y$_\square$ slightly move towards Cu

Table 1
Comparison of Interatomic distance (in Å) between the atoms of CuYO$_2$ with its defects (where 'M' denotes the defect atom).

Compounds	Cu–O	Y–O	Cu-O$_i$	Y-O$_i$	M-O	M-O$_i$
Ideal Cell	1.832	2.304	–	–	–	–
O$_i$	1.833	2.290	2.056 (3)	2.570 (2)	–	–
Y$_\square$	1.763	2.267	–	–	2.597	–
B$_Y$	1.833	2.395	–	–	1.865 (6)	–
B$_Y$ + O$_i$	1.838 (3) 1.859 (3)	2.394	1.936 (3)	2.296	1.865 (6)	3.082
Al$_Y$	1.835	2.357	–	–	2.024 (6)	–
Al$_Y$ + O$_i$	1.845 (3) 1.859 (3)	2.364	1.969 (3)	2.337	2.058 (3)	3.094
Ga$_Y$	1.833	2.342	–	–	2.101 (6)	–
Ga$_Y$ + O$_i$	1.842 (3) 1.856 (3)	2.344	1.974 (3)	2.355	–	3.063
In$_Y$	1.832	2.315	–	–	2.256 (6)	–
In$_Y$ + O$_i$	1.841 (3) 1.849 (3)	2.309	2.004 (3)	2.879	2.259 (6)	2.879

and Y atoms to attract more electrons. Furthermore, in the substitutional defects, the distance between M-O in MO$_6$ (M = B, Al, Ga, and In) octahedra is shown to increase linearly with the ionic radius of the substituted atoms. In concurrence with Ref. [15], the size of the substituted trivalent cation affects the Cu-O$_i$ distance in the defect complexes. Herein the substituted defects increase the Cu-O$_i$ distance linearly according to their ionic radius, implying that the larger trivalent cations facilitate more space for O$_i$ than the smaller one.

3.4. Defect formation energy calculations

The equation for calculating the formation energy of a defect X in the charge state q is expressed as [49,50]

$$E^{form}[X^q] = \left\{ E_{tot}[X^q] + E_q^{corr} \right\} - E_{tot}[pristine] - \sum_i n_i \mu_i + q\left(E_v + E_f - \Delta V_{0/p}\right)$$

where, $E_{tot}[X^q]$ is the total energy of supercell with defect X in the charge state q, $E_{tot}[pristine]$ is the total energy of pristine supercell, n_i is a number of atoms of type i are added (+ve) or removed (-ve), μ_i is the chemical potential of an atom (type i), E_v is the valence band maximum (VBM) of the pristine cell, E_f is Fermi-energy, E_q^{corr}, and $\Delta V_{0/p}$ are the correction terms calculated by CoFFEE package [42].

The calculated formation energies of neutral defects and defect complexes are plotted (see Fig. 3) against the various stability points defined by the stability diagram (see Fig. 1). The considered defects and defect complexes are favourable to occur only at Oxygen-rich conditions, except for the defects Y$_\square$, B$_Y$, and B$_Y$ + O$_i$. The Yttrium vacancy
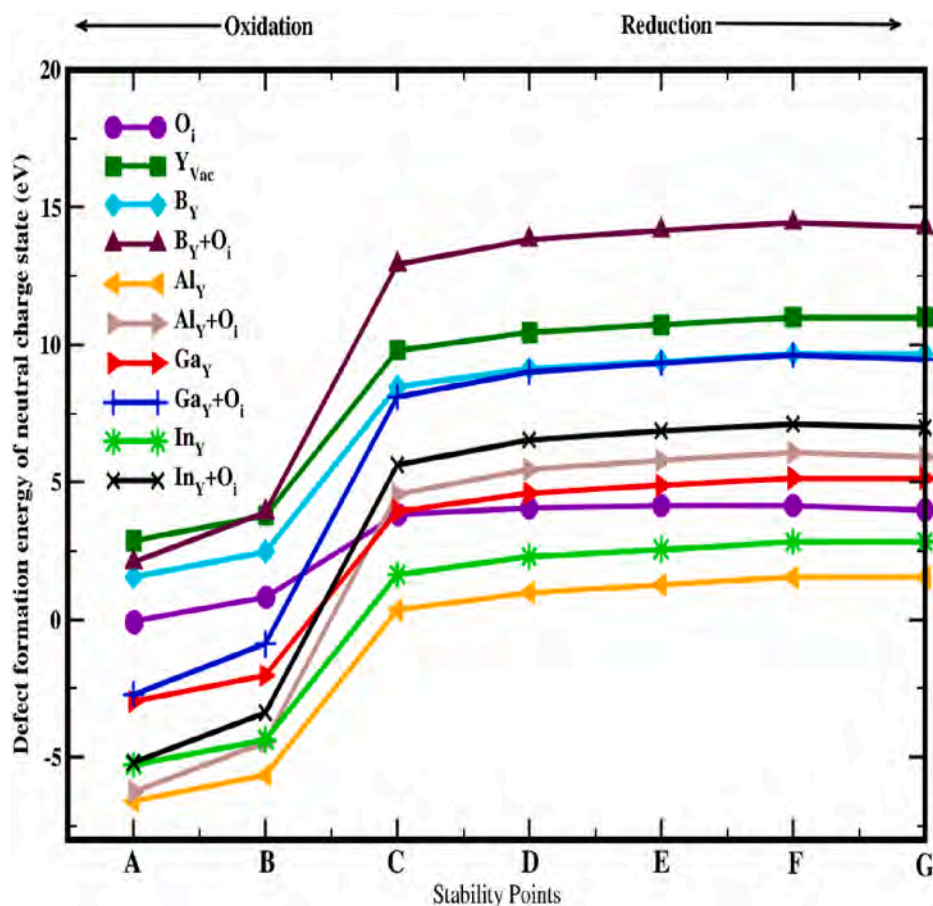
Fig. 3. Defect formation energy for various neutral defects as well as their defect complexes (Oxidation and reduction conditions also depicted) against the stability points determined from Fig. 1.

creates more local distortion, and also it disturbs nearby YO_6 octahedral coordination. Similarly, in B substitution, the small ionic radius of B and its large electronegativity also creates considerable local distortion compared to the other substituted defects and their complexes, which decreases the stability as indicated in Fig. 3. At O rich conditions, the defect formation energies of substituted defects and their complexes are almost similar. On the other hand, at O-poor conditions, the formation energy of the above defects increases to positive values implying that the defect complex cannot form at such Oxygen poor conditions. So, the Oxygen-rich condition is essential to create the O_i and other defect complexes, and previously, it has been shown that experimentally $CuYO_2$ thin films could be oxidized by heating $CuYO_2$ in the O_2 environment [11,15,24]. Hence, the Oxygen-rich condition helps to stabilize the defect complexes. Hereafter, the defects and their defect complexes will be focused on which are more favourable to occur.

The formation energy of the defect O_i and defect complexes $B_Y + O_i$, $Al_Y + O_i$, $Ga_Y + O_i$, and $In_Y + O_i$ has been calculated with respect to the Fermi energy starting from VBM to CBM. The VBM and CBM values are taken from HSE corrected band edge positions. These formation energies are calculated for the high stability points (the corners of the stability region) in the phase diagram of CuYO2 (Fig. 1) by considering the possible charge states for O_i. It may be recalled that the chemical potential of the elements Cu, Y, and O with respect to the chemical potential of the corresponding precursor materials. Herein, the Oxygen-rich as well as the metal-rich conditions are imposed as depicted in Fig. 1 and compared with each other (see Fig. 4a, b, 4c, and 4d). As discussed in the neutral case, the Oxygen-rich condition is more favourable for the charged defects. The metal-rich conditions have negative defect formation energy at the charge state of -2 when the

Fermi energy value is near CBM. As this is less significant for hole formation, the discussion here is restricted to the Oxygen-rich conditions alone.

In the neutral case, $B_Y + O_i$ shows positive defect formation energy, which is greater than that of O_i. But, the charge states -1 and -2 were shown to have a negative defect formation energy indicating that shallow transition from neutral to -1 charge state occurred below VBM, which is advantageous and eventually enhances the p-type conductivity. Moreover, $Ga_Y + O_i$ and $Al_Y + O_i$ defect complexes exhibit the same shallow transition states. Hence, the p-type conductivity could be improved by co-doping B, Al, and Ga with O_i. At the same time, co-doping with In_Y and O_i, deep transition states as in the case of O_i were created. Herein, the ionic radius of In is comparable to Y, also Y-O_i and In-O_i distances are identical, but the X-O_i (X = B, Al, and Ga) distance is larger than that of Y-O_i. Hence, large distortion while co-doping O_i with X (X–B, Al, and Ga) leads to shallow charge state transitions. On the other hand, the charge state transitions of defect complexes other than the defects mentioned above occur in the middle of the bandgap. Those are called deep levels (or deep trap), which decreases the conductivity. These deeper levels may help to fix the Fermi level far from the band edges [49]. Hence this can be used as an insulating buffer layer in electronic devices and generate monochromatic laser.

3.5. Electronic structure and density of states

Fig. 5a and b shows the site projected electronic band structures (Cu-d_z^2 and O-p_z orbital states, respectively) of pristine $CuYO_2$ along with the high symmetry points in the first Brillouin zone. An indirect bandgap of 2.6 eV from H to Γ point is seen, which is, however, underestimated
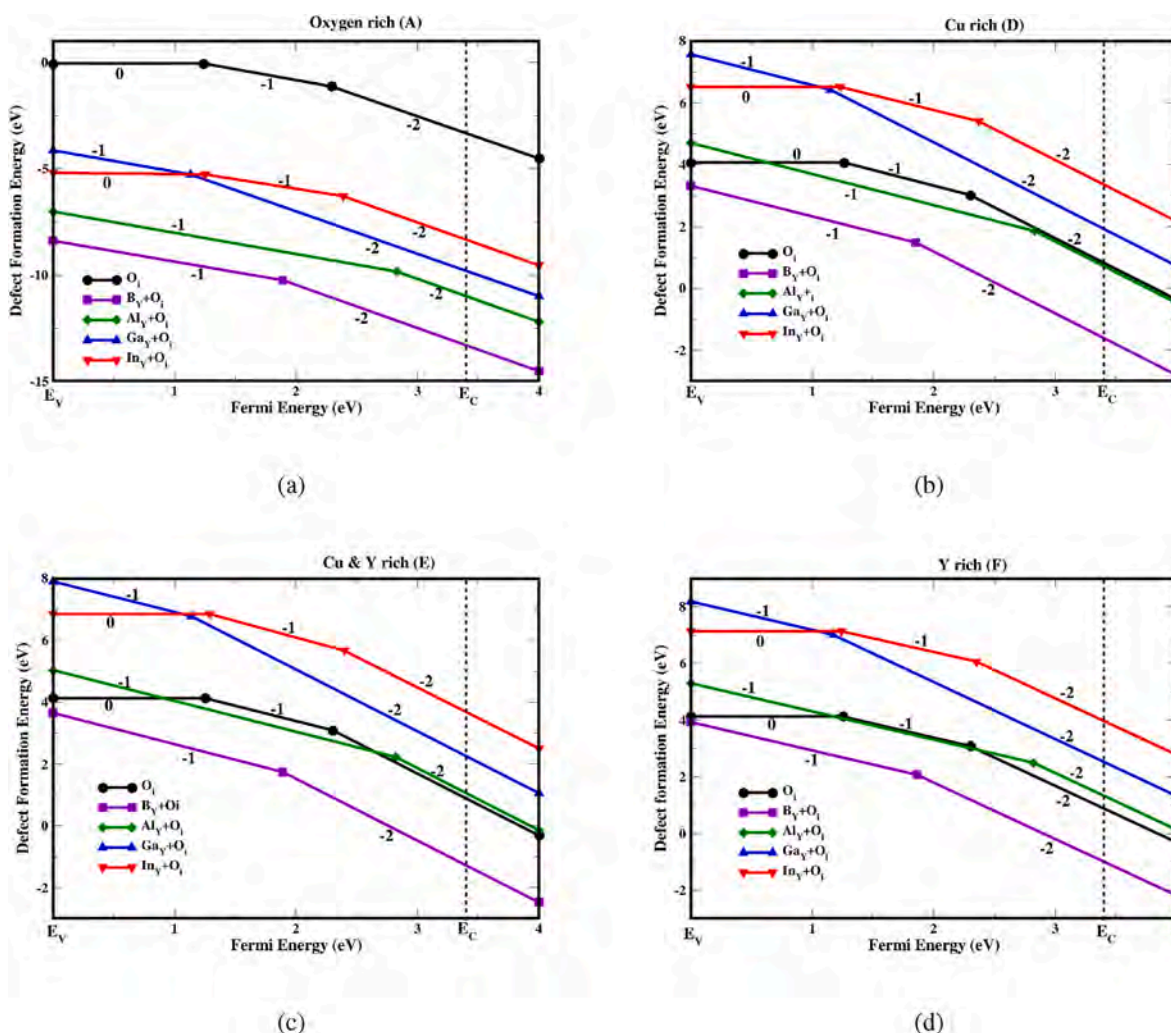
Fig. 4. Defect formation energy of O_i and defect complexes at different charge states that are calculated with respect to the Fermi energy (E_F), for the most stable composition taken from the phase-stability diagram (Fig. 1).

compared to the experimental band gap of 3.5–3.8 eV[51–54]. A previous theoretical study using the full potential-linear muffin-tin orbitals (FP-LMTO) method obtained an E_g of 3.3 eV [28]. But our calculated band gap value is consistent with the previous pseudo-potential based first-principles calculations [29,31]. Accuracy in the bandgap of pristine $CuYO_2$ was improved with our HSE calculation (see Fig. 5c), which yields a bandgap of 3.4 eV, in good agreement with the experimental band gap values [51,53,54] and with theoretical calculations using FP-LMTO [28]. The GGA calculated bandgaps of other defect complexes of $CuYO_2$ were corrected with the help of a scissor operator (the difference between the bandgaps of pristine $CuYO_2$ calculated using HSE and GGA). Hereafter, the expressed band gap values are computed using GGA and corrected with the help of a scissor operator.

The GGA calculated DOS and atomic projected band structures (see Fig. S2) show that the valence band extends from −1 eV to −6.5 eV, in which the Cu-d orbital states dominate from −3 eV to −1 eV. In contrast, the O-p orbital states dominate from −3 eV to −6.5 eV energy range. Similar to that, the calculated site projected band structures (see Fig. 5a and b, S4(a), S4(b)) of pristine $CuYO_2$ shows that the VBM consists mostly of Cu-d_{z^2} and non negligible Cu-s, O p_y, and p_z orbital states. Energetic and spatial degeneracy between Cu-d_{z^2} and O-p_z orbital states in the VBM corroborates the probability of non-negligible hybridization between those states. Herein, the Cu-d_{z^2} orbital de-localizes the O-p orbitals, which enhances the p-type conductivity in $CuYO_2$ as described earlier work [13]. Below VBM, there is also a possible non-negligible

hybridization between Cu-$d_{x^2-y^2}$ and O-p_x orbital states. This hybridization leads to the sharing of electrons and elucidates non-negligible covalent interaction between Cu and O atoms. There are no such degenerate energy states between Y and O, implying that Y has donated most of its electrons to O and forms significant ionic bonding with Oxygen. Due to the contribution from the s orbital states of Cu, Y, and O (see Figs. S4(a) and S4(c), and S4(d)) with Cu-d_{z^2} orbital state, CBM is more dispersed than the VBM leading to good electronic conductivity rather than the hole conductivity. This transparent nature, along with the good electrical property of $CuYO_2$, can facilitate its applications in solar cells as transparent contacts, touch displays, and window layers.

The plotted band structure of $CuYO_2$ supercell with O_i (see Fig. 6a) shows an indirect bandgap of 2.92 eV between H and Γ points after the application of a scissor operation (see section 3.5). This bandgap is more favourable to absorb the violet region of the electromagnetic spectrum (see Fig. 7). These energy levels introduced by O_i are mainly composed of O_i-p_x, O_i-p_y (see Figs. S5(c) and S5(d)), Cu-d_{xy}, and Cu-d_{z^2} (see Figs. S5 (a) and S5(b)) orbital states. Here also there is a possibility of hybridization between O_i-p_x or O_i-p_y and Cu-d_{xy} orbital states. As the O_i is an acceptor dopant, the empty conduction band states) are not affected. The created $Y_\square$ in pristine $CuYO_2$ (see Fig. S3(d)) slightly moves the CBM of pristine $CuYO_2$ away from the Fermi level and negligibly increases the band gap value. Which also modifies the indirect bandgap of $CuYO_2$ into the direct bandgap along with the Γ point. Even though the $Y_\square$ changes the indirect bandgap to a technologically important direct
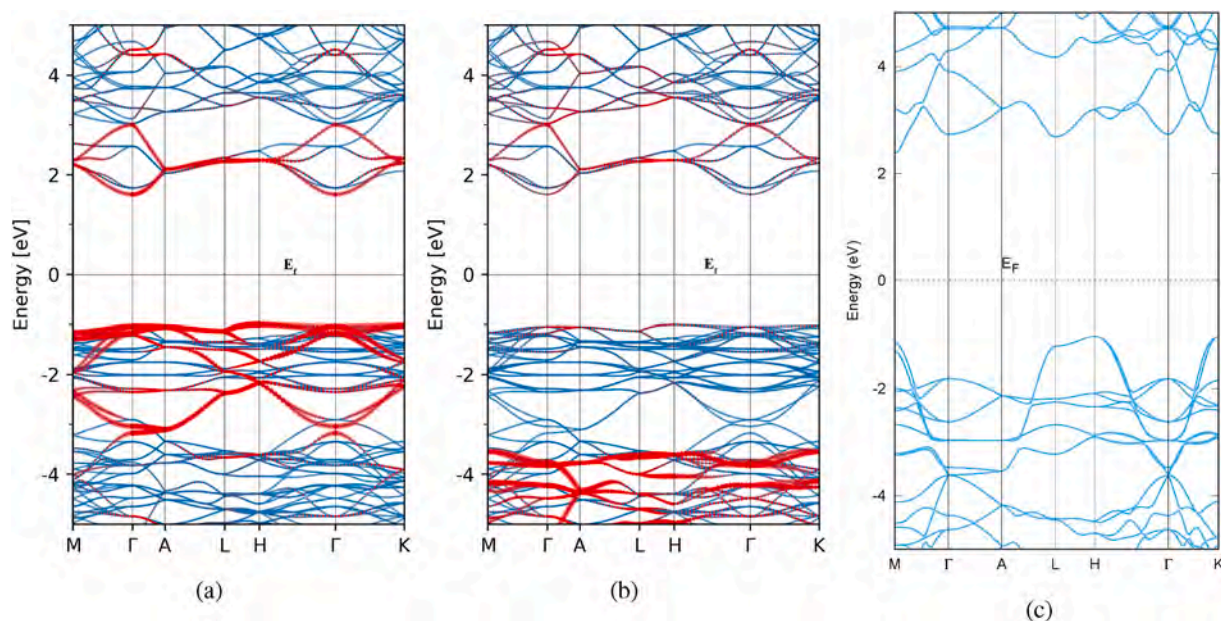
Fig. 5. Orbital projected band structure of CuYO$_2$ (a) Cu d_{z^2} orbital calculated using GGA, (b) O p_z orbital (projected as red colour) calculated using GGA, (c)HSE calculated band structure of pristine CuYO$_2$. (For interpretation of the references to colour in this figure legend, the reader is referred to the Web version of this article.)
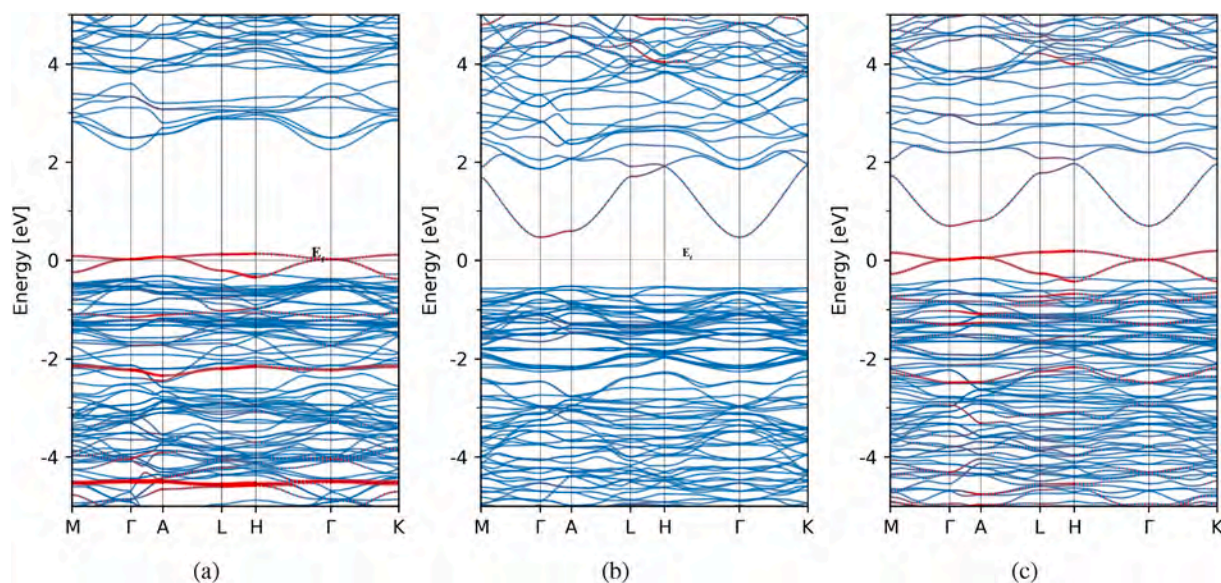
Fig. 6. Electronic band structure of CuYO$_2$ supercell with (a.) interstitial Oxygen (O$_i$ states are projected in red colour) (b.) B$_Y$ (B states are projected in red colour) (c.) B$_Y$ + O$_i$ (both B and O$_i$ states are projected in red colour). (For interpretation of the references to colour in this figure legend, the reader is referred to the Web version of this article.)

bandgap nature, creating Y$_\square$ in CuYO$_2$ is not spontaneous according to the formation energy calculated in this work (see Fig. 3).

The GGA calculated electronic band structures of CuYO$_2$ with B$_Y$ (see Fig. 6b) shows that the created defect levels are closer to CBM, due to which the bandgap becomes 1.81 eV. Whereas the electronic band structure of B$_Y$ + O$_i$ (see Fig. 6c) defect complex of CuYO$_2$ elucidates the modified VBM as well as CBM, which again narrows down the bandgap to 1.08 eV. These bandgaps of CuYO$_2$ with B$_Y$ and B$_Y$ + O$_i$ were inferred as 1.81 eV and 1.08 eV, respectively, with the help of a scissor operator to estimate its real bandgap. This narrow bandgap elucidates their capability of absorbing low-energy photons. The B substitution does not make any significant change in VBM, but CBM becomes more dispersed than that of the pristine supercell. The change in CBM is due to the

traceable s orbital states of B (see Fig. 6b) and O (see Fig. S6(a)), d_{xz} and d_{yz} orbital states of Y (Fig. S6(b) and S6(c)) and also a small contribution from Cu d_{z^2} (see Fig. S6(d)) orbital states.

The band gaps of CuYO$_2$ supercell with Al$_Y$, Al$_Y$ + O$_i$, Ga$_Y$, Ga$_Y$ + O$_i$, In$_Y$, and In$_Y$ + O$_i$ are obtained (2.66 eV, 2.29 eV, 2.45 eV, 2.06 eV, 1.70 eV, and 1.96 eV, respectively) from the GGA calculated band structure of respective supercells (see Fig. S7(a), (b), S8(a), (b), S9(a), and (b), respectively). All of these substitutional defects depict that the bottom-most conduction band is mostly composed of s orbital states of corresponding substituted atoms such as Al or Ga or In and Y-d_{xz} and Y-d_{yz} orbitals states. Also, there is a small contribution from Cu-d_{z^2} and O-s orbital states. The s orbital contribution from the substituted atom increases (in the order of B<Al<Ga<In) at CBM with the ionic radii of the
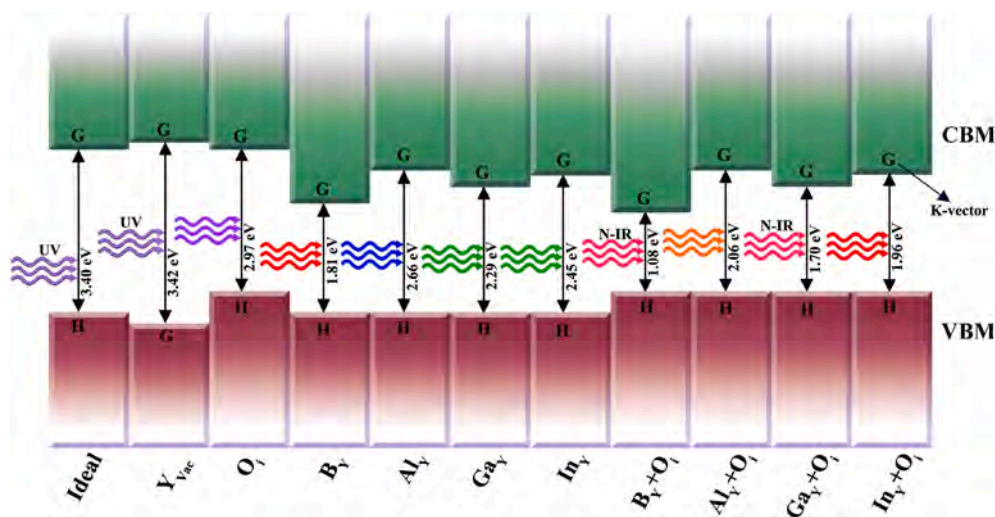
Fig. 7. Schematic diagram of band edge positions of CuYO$_2$ (with and without defects) and corresponding HSE corrected band gap with their absorption ranges.

substituted atom. Hence, this implies that larger ionic radii facilitate more hybridization between s orbital of substituent atoms and d orbitals of Y, thereby increasing the dispersion of CBM from B to In. This dispersed nature of CBM is advantageous to the negative charge carriers, and the material can be doped as an n-type semiconductor. The schematic diagram illustrating the band edge positions of all defect complexes is shown in Fig. 7), with respect to absorption regions of the electromagnetic spectrum. The transparency of CuYO$_2$ is not increased due to these substitutions of B, Al, Ga, and In at the Y site as expected. This electronic structure calculation elucidates that the VBM and CBM of CuYO$_2$ can be tuned with suitable defects and proposes new ways for bipolar doping in CuYO$_2$.

3.6. Effective mass

The GGA calculated band structures were used to evaluate the effective mass of pristine and defect complexes of CuYO$_2$. The finite difference method was employed to evaluate the second derivative of E-K relation at extrema points and given in Table 2. The calculated effective mass of holes in CuYO$_2$ is consistent with the available theoretical results by using polynomial fitting [48]. However, hitherto no reports available on the effective masses of the defect complexes.

The dispersed nature of CBM rather than VBM in the calculated band structures of pristine and supercells with defects suggests that the electrons might have more mobility than that of holes. Calculated effective mass (see Table 2) also confirms the same, whereas the electron effective mass of pristine supercell is lower in the direction of $\Gamma - H$ compared to that of holes. The interstitial Oxygen increases the p orbital contribution to VBM, reducing the dispersion of energy bands at VBM and leading to increased effective mass compared to that of pristine CuYO$_2$. Even though the experimental results indicated that the CuYO$_2$
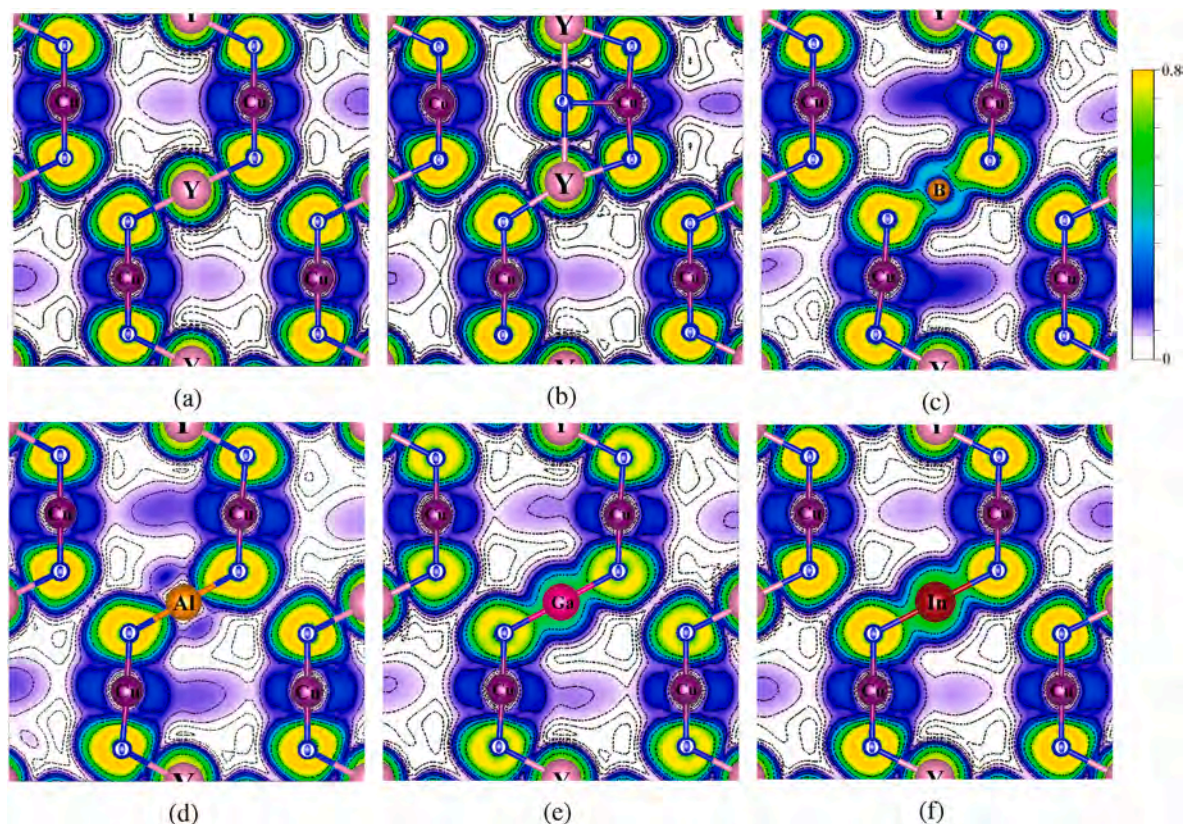
has naturally occurring p-type conductivity [38, 41, 25], the p-type conductivity increases with O$_i$ defect [5, 33]. Conversely, the effective mass shows no sign of increasing p-type conductivity with O$_i$. However, the defect concentration in the experimental case could be more than that in modeling, which can cause enhanced conductivity of charge carriers. The substituted defects in CuYO$_2$ reduce the effective mass of an electron, where the defects with B$_Y$ and Ga$_Y$ have the lowest electron effective masses compared to other defect complexes, and this results in high electronic conductivity. In accordance with the band structure calculations, the effective mass calculations also confirm the possibility of bipolar doping in CuYO$_2$.

3.7. Electronic charge distribution

The charge density (see Fig. S15) and electron localization functions (ELF) (see Fig. 8) were calculated along the (110) planes for pristine and defect complexes of CuYO$_2$. Both the calculated charge density (see Fig. S15) and ELF (see Fig. 8a) confirm that the bonds between Cu–O and Y–O are mostly ionic with non-negligible covalent character in consonance with partial DOS. The Cu–O bonds have more covalent characteristics than the Y–O bonds. These results contradict the previous calculations from Born effective charges by using LDA, which shows that the Y–O bond is more covalent than the Cu–O bond [46,47]. Moreover, the slight electronegativity difference between Cu–O (1.60) compared to that between Y–O (2.28) is also consistent with the above results. Charge density (Fig. S15) and ELF (see Fig. 8b) plots of CuYO$_2$ supercell with O$_i$ shows that the O$_i$ in the Cu plane shares an electron with Cu, and also it attracts electrons from Y atoms present above and below. Therefore the Y and Cu atoms are slightly moved closer to O$_i$, clearly seen in the ELF plot.

A small local distortion is observed from the ELF plots of CuYO$_2$ supercell with B$_Y$ (see Fig. 8c), Al$_Y$ (see Fig. 8d), Ga$_Y$ (see Fig. 8e) and In$_Y$ (see Fig. 8f). Compared to other substituents, the O–Cu–O linear chain is more distorted in B-doped CuYO$_2$, owing to the large electronegativity of B. Even though homogeneous electron density can be seen around B from ELF, the small ELF lobe extended from O towards B implies that the electrons get pulled towards it, implying that the B–O bond mixes both ionic and covalent characters. Due to the small electronegativity, Al has donated most of its electrons to O and modifies the electronic environment of O (see Fig. 8d). Hence, the bonding between Al–O is mostly ionic with a non-negligible polar covalent character. Due to the large ionic radius of Ga and In compared to that of B and Al, a small local distortion is observed in Ga$_Y$, and In$_Y$ substituted CuYO$_2$ (see Fig. 8e and f). The homogeneous electronic distribution between Ga–O and In–O is seen

Table 2
Calculated effective mass in the unit of m$_o$ for CuYO$_2$ (with and without defects).

Compounds	Effective Mass (m*)			
	Hole		Electron	
	Γ-A	Γ-H	Γ-K	Γ-H
Ideal Cell	0.79	1.38	0.94	0.60
O$_i$	1.05	2.53	0.93	0.65
Y$_\square$	1.30	1.31	0.88	0.60
B$_Y$	1.71	3.56	0.40	0.58
Al$_Y$	1.83	3.37	0.51	0.63
Ga$_Y$	1.25	2.46	0.43	0.58
In$_Y$	1.17	2.55	0.50	0.66

Fig. 8. Calculated electron localization functions of (a.) CuYO$_2$ and the super cell CuYO$_2$ with (b.) O$_i$ (c.) B$_Y$ (d.) Al$_Y$ (e.) Ga$_Y$ (f.) In$_Y$ are plotted along 110 plane.

from the plotted ELF implies that the bonds are mostly covalent. The large ionic radius of In compared to B, Al and Ga enable the covalent interaction with O$_i$, which is observed in the plotted charge densities and ELFs of CuYO$_2$ supercell with defect complexes. The local distortion is observed in all defect complexes and decreases from B to In. This local distortion created by the defects leads to the splitting of an energy level and gives rise to the intermediate states or deep levels in the bandgap. These deep levels may act as colour centers or might be useful for up-conversion, which is important in the luminescent properties of the materials.

3.8. Optical properties

The optical response of the material is derived from the frequency-dependent complex dielectric function $\varepsilon(\omega) = \varepsilon_1(\omega) + i\varepsilon_2(\omega)$. The imaginary part of the dielectric function $[\varepsilon_2(\omega)]$ is calculated by summing over the empty band states [55], and the real part $[\varepsilon_1(\omega)]$ is calculated from $\varepsilon_2(\omega)$ via Kramers-Kronig transformation. Due to the hexagonal symmetry, CuYO$_2$ has two independent components of ε_1 and ε_2. The components perpendicular (E $\perp$c) and parallel (E $\parallel$c) to z-axis are denoted as ε_1^{xx} and ε_1^{zz}, respectively for real part of $\varepsilon(\omega)$, and also ε_2^{xx} and ε_2^{zz}, respectively for imaginary part of $\varepsilon(\omega)$. The static dielectric constant of 5.33 and 4.64 was obtained for x and z components of ε_1 (see Fig. 9a),
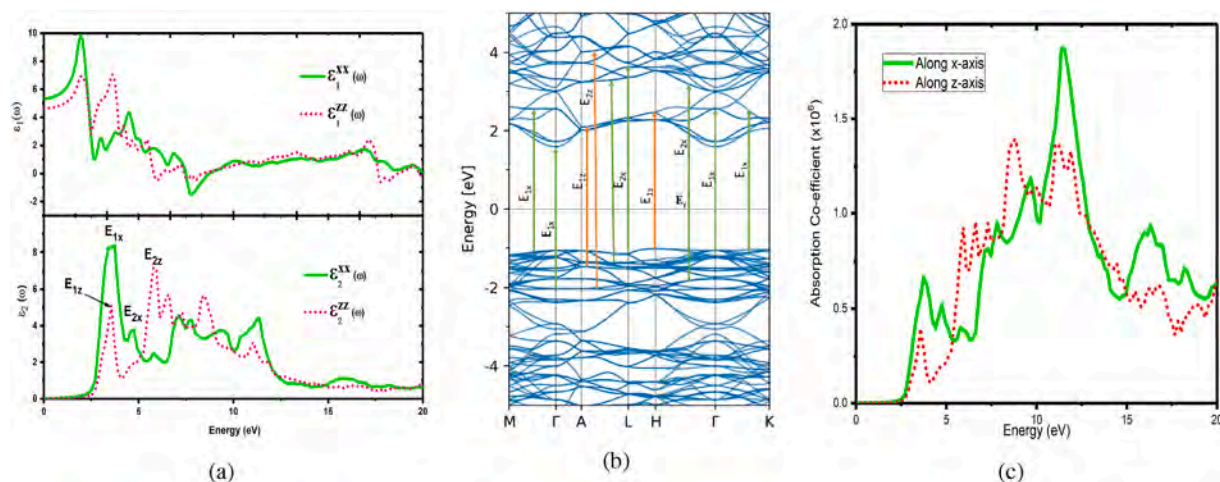
Fig. 9. Calculated (a) Real and Imaginary dielectric tensors of CuYO$_2$, (b) Possible transitions are represented in the band structure corresponding to the peaks in ε_2, (c) Absorption co-efficient of CuYO$_2$.

respectively, are consistent with the previously calculated values of 5.47 and 4.72 [47]. The large value of the dielectric constant indicates the good absorptive nature of $CuYO_2$. In particular, the dielectric response to the electric field of the components E $\perp$c and E $\parallel$c at low frequencies is significant. However, both real and imaginary parts of the dielectric constant become frequency-independent at high frequencies.

Both x and z components of ε_2 show that the absorption starts at the energy range of 2.6 eV, which is consistent with the band gap obtained using GGA. The absorptive peaks in ε_2 are represented by the transitions from the valence band to the conduction band. The possible allowed transitions giving rise to the peaks in ε_2 are derived from the band structure and plotted along with ε_2 (see Fig. 9b). The high peak (E_{1x}) at 3.73 eV is mostly corresponding to the transitions between the orbital states of Cu d at VBM and O p at CBM, Cu s at VBM and O p or Cu p at CBM, Cu d_{xy} or $d_{x^2-y^2}$ at VBM and Y s at CBM, O p_z at VBM and Cu s or d_{z^2} or Y $d_{x^2-y^2}$ at CBM. The transitions between the orbital states O p at VBM and Cu or Y d at CBM, Cu s at VBM and Cu or O p_y at CBM, Cu d and O p_z or s, Cu d and Y s orbital states are mainly responsible for the peak (E_{1z}) at 3.56 eV. Small peak (E_{2x}) at 4.75 is mostly corresponding to the transitions between Cu s and Cu p_y or O p_y, O p_z and Cu or Y d_{z^2}, O p and Y d orbital states. The peak (E_{2z}) at 5.9 eV represents the transitions between Cu d and O s, Cu d and O p_z, Cu d and Y s orbital states. The transitions from O p and Cu d into the conduction band states are mainly responsible for absorptive nature of $CuYO_2$.

These real and imaginary dielectric tensors are used to calculate the absorption coefficient (see Fig. 9c), energy loss spectrum, extinction co-efficient, reflectivity and refractive index (see Fig. 10). Both components of absorption co-efficient show good absorption up to 13 eV energy range. The surface perpendicular to the z-axis has good optical absorption rather than that parallel to the z-axis. A positive extinction coefficient value indicates good attenuation of the incident electromagnetic wave. The peaks in the absorption coefficient correlate with the extinction coefficient, implying that $CuYO_2$ completely absorbs the incident photons. The material shows 15% reflection to the low energy

photons, while the reflectivity increases up to 35% for high energy photons. The obtained refractive indices of 2.31 and 2.15 (along $\perp$ and $\parallel$, respectively to the z-axis) are consistent with the previously calculated theoretical value of 2.34 and 2.17 [47]. The calculated square of the refractive index is substantially equal to the static dielectric constant, implying that the material has more electronic contribution to the static dielectric constant than the ionic contribution. This also confirms the existence of the covalent nature of bonding in $CuYO_2$. These high refractive indices indicate low light reflection loss at the interface. Furthermore, the small energy loss function also confirms the same. All these properties of $CuYO_2$ point out that it can be used as a potential absorption and window material in solar cells.

4. Conclusions

The first-principles calculations were employed to study the effect on the electronic properties of $CuYO_2$ with different types of defects and their defect complexes. Further, analyzed the stable phase of $CuYO_2$ and its consequences in the defect formation energy, in which the Oxygen-rich condition is more suitable for creating the defects such as interstitial Oxygen (O_i), Yttrium vacancy ($Y_\square$), Yttrium substituted by B, Al, Ga and In (B_Y, Al_Y, Ga_Y, and In_Y) and defect complexes (Yttrium substituents together with Oxygen interstitial). Initially, the calculation aimed to increase the transparency and conductivity by substituting the IIIA trivalent cations instead of IIIB trivalent cation along with O_i. The results obtained in this work also shown to decrease the transparency due to the combination of defects such as interstitial Oxygen (O_i), Yttrium substituted by B, Al, Ga and In (B_Y, Al_Y, Ga_Y, and In_Y) and defect complexes (Yttrium substituents together with Oxygen interstitial). But, co-doping of B_Y with O_i substantially improves the p-type conductivity. Again, the band edge positions are tuned so that $CuYO_2$ can absorb low-energy photons and high-energy photons. Instead of transparency, the substitutional defects enhance the electronic conductivity, and also the materials have the capability of bipolar doping. Finally, our calculations
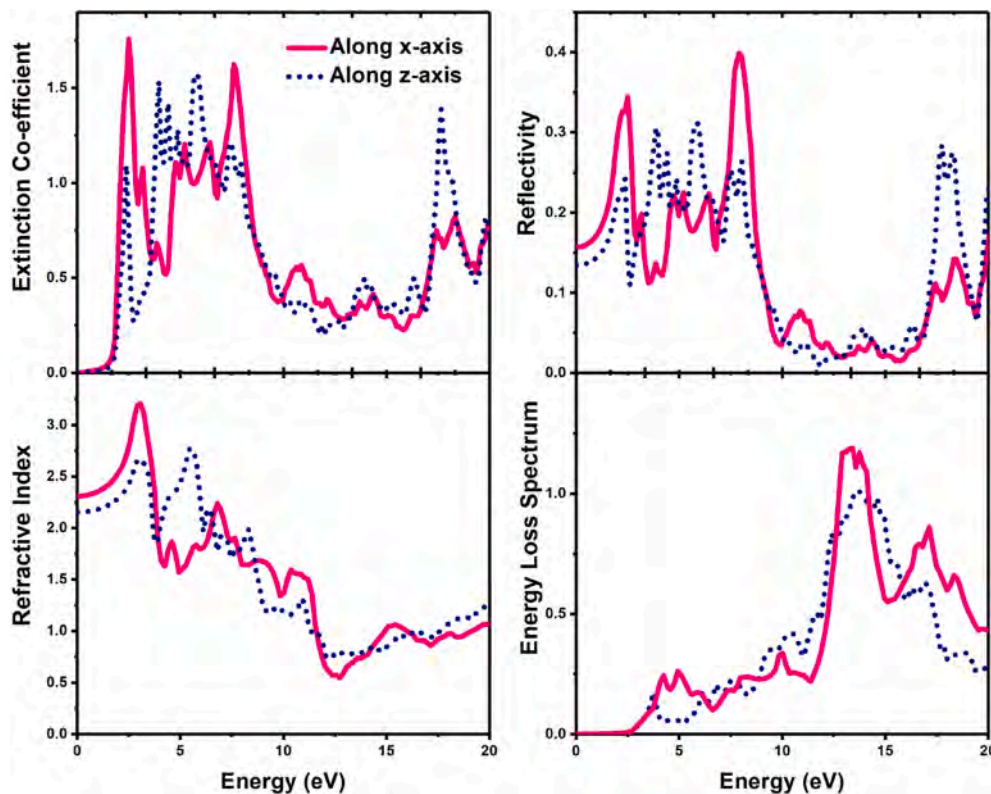

Fig. 10. Calculated Extinction co-efficient, Reflectivity, Refractive index and Energy loss spectrum of $CuYO_2$ using GGA.

depict that, $CuYO_2$ with suitable defects could absorb the particular range of energy as needed. Also, transparent nature in pure form may be used as window material and transparent contacts in solar cells.

CRediT authorship contribution statement

T. Premkumar: Data curation, Formal analysis, Writing – original draft, Collected the data, Contributed data or analysis tools, Performed the analysis, Wrote the paper. **R. Vidya:** Data curation, Formal analysis, Writing – original draft, Contributed data or analysis tools, Performed the analysis, Wrote the paper. **Helmer Fjellvåg:** Formal analysis, Writing – original draft, Conceived and designed the analysis, Performed the analysis.

Declaration of competing interest

The authors declare that they have no known competing financial interests or personal relationships that could have appeared to influence the work reported in this paper.

Acknowledgements

Appendix A. Supplementary data

Supplementary data to this article can be found online at https://doi.org/10.1016/j.matchemphys.2022.126101.

References

[1] D.S. Ginley, C. Bright, Transparent conducting oxides, MRS Bull. 25 (2000) 15–18, https://doi.org/10.1557/mrs2000.256.
[2] T. Minami, Transparent conducting oxide semiconductors for transparent electrodes, Semicond. Sci. Technol. 20 (2005) S35–S44.
[3] E. Fortunato, D. Ginley, H. Hosono, D.C. Paine, Transparent conducting oxides for photovoltaics, MRS Bull. 32 (2007) 242–247.
[4] R.G. Gordon, Criteria for choosing transparent conductors, MRS Bull. 25 (2000) 52–57, https://doi.org/10.1557/mrs2000.151.
[5] Kate G. Godinho, A. Walsh, G.W. Watson, Energetic and electronic structure analysis of intrinsic defects in SnO_2, J. Phys. Chem. C 113 (2009) 439–448.
[6] A. Walsh, J.L.F. Da Silva, S.H. Wei, C. Körber, A. Klein, L.F.J. Piper, A. DeMasi, K. E. Smith, G. Panaccione, P. Torelli, D.J. Payne, A. Bourlange, R.G. Egdell, Nature of the band gap of in_2o_3 revealed by first-principles calculations and x-ray spectroscopy, Phys. Rev. Lett. 100 (2008), 167402.
[7] B.G. Lewis, D.C. Paine, Applications and processing of transparent conducting oxides, MRS Bull. 25 (2000) 22–27.
[8] A.F. Kohan, G. Ceder, D. Morgan, C.G. Van de Walle, First-principles study of native point defects in ZnO, Phys. Rev. B 61 (2000) 15019–15027.
[9] G. Thomas, Invisible circuits, Nature 389 (1997) 907–908.
[10] F. Benko, F. Koffyberg, Opto-electronic properties of p- and n-type delafossite, $CuFeO_2$. J. Phys. Chem. Solids 48 (1987) 431–434.
[11] R. Cava, H. Zandbergen, A. Ramirez, H. Takagi, C. Chen, J. Krajewski, W. Peck, J. Waszczak, G. Meigs, R. Roth, L. Schneemeyer, $LaCuO_{2.5+x}$ and $CuYO_{2.5+x}$ delafossites: materials with triangular $Cu^{2+\delta}$ planes, J. Solid State Chem. 104 (1993) 437–452.
[12] N. Duan, A.W. Sleight, M.K. Jayaraj, J. Tate, Transparent p-type conducting $CuScO_{2+x}$ films, Appl. Phys. Lett. 77 (2000) 1325–1326.
[13] H. Kawazoe, M. Yasukawa, H. Hyodo, M. Kurita, H. Yanagi, H. Hosono, P-type electrical conduction in transparent thin films of $CuAlO_2$, Nature 389 (1997) 939–942.
[14] R. Nagarajan, A.D. Draeseke, A.W. Sleight, J. Tate, p-type conductivity in $CuCr_{1-x}Mg_xO_2$ films and powders, J. Appl. Phys. 89 (2001) 8022–8025.
[15] R. Nagarajan, N. Duan, M. Jayaraj, J. Li, K. Vanaja, A. Yokochi, A. Draeseke, J. Tate, A. Sleight, p-type conductivity in the delafossite structure, Int. J. Inorg. Mater. 3 (2001) 265–270.
[16] M. Sasaki, M. Shimode, Fabrication of bipolar $CuInO_2$ with delafossite structure, J. Phys. Chem. Solid. 64 (2003) 1675–1679.
[17] M. Snure, A. Tiwari, $CuBO_2$: a p-type transparent oxide, Appl. Phys. Lett. 91 (2007), 092123.
[18] J. Tate, M. Jayaraj, A. Draeseke, T. Ulbrich, A. Sleight, K. Vanaja, R. Nagarajan, J. Wager, R. Hoffman, p-type oxides for use in transparent diodes, Thin Solid Films 411 (2002) 119–124.
[19] C.W. Teplin, T. Kaydanova, D.L. Young, J.D. Perkins, D.S. Ginley, A. Ode, D. W. Readey, A simple method for the preparation of transparent p-type Ca-doped $CuInO_2$ films: pulsed-laser deposition from air-sintered Ca-doped $Cu_2In_2O_5$ targets, Appl. Phys. Lett. 85 (2004) 3789–3791.
[20] H. Yanagi, S.i. Inoue, K. Ueda, H. Kawazoe, H. Hosono, N. Hamada, Electronic structure and optoelectronic properties of transparent p-type conducting $CuAlO_2$, J. Appl. Phys. 88 (2000) 4159–4163.
[21] D.B. Rogers, R.D. Shannon, C.T. Prewitt, J.L. Gillson, Chemistry of noble metal oxides. iii. electrical transport properties and crystal chemistry of ABO_2 compounds with the delafossite structure, Inorg. Chem. 10 (1971) 723.
[22] B.J. Ingram, B.J. Harder, N.W. Hrabe, T.O. Mason, K.R. Poeppelmeier, Transport and defect mechanisms in cuprous delafossites.2, $CuScO_2$ and $CuYO_2$. Chem. Mater 16 (2004) 5623–5629.
[23] R.S. Yu, S.C. Liang, C.J. Lu, D.C. Tasi, F.S. Shieu, Characterization and optoelectronic properties of p-type n-doped $CuAlO_2$ films, Appl. Phys. Lett. 90 (2007), 191117.
[24] R. Manoj, M. Nisha, K.A. Vanaja, M.K. Jayaraj, Effect of oxygen intercalation on properties of sputtered $CuYO_2$ for potential use as p-type transparent conducting films, Bull. Mater. Sci. 31 (2008) 49–53.
[25] D. Kim, S. Park, E. Jeong, H. Lee, S. Choi, Optical and electrical properties of p-type transparent conducting $CuAlO_2$ thin film, Thin Solid Films 515 (2007) 5103–5108.
[26] A. Buljan, P. Alemany, E. Ruiz, Electronic structure and bonding in $CuMO_2$ (M = Al, Ga, Y) delafossite-type oxides: an ab initio study, J. Phys. Chem. B 103 (1999) 8060–8066.
[27] B.J. Ingram, T.O. Mason, R. Asahi, K.T. Park, A.J. Freeman, Electronic structure and small polaron hole transport of copper aluminate, Phys. Rev. B 64 (2001), 155114.
[28] L.J. Shi, Z.J. Fang, J. Li, First-principles study of p-type transparent conductive oxides $CuXO_2$ (X=Y, Sc, and Al), J. Appl. Phys. 104 (2008), 073527.
[29] M.N. Huda, Y. Yan, A. Walsh, S.H. Wei, M.M. Al-Jassim, Group-iiia versus iiib delafossites: electronic structure study, Phys. Rev. B 80 (2009), 035205.
[30] Z.J. Fang, L.J. Shi, First-principle study of extrinsic defects in $CuScO_2$ and $CuYO_2$, Phys. Lett. 372 (2008) 3759–3762.
[31] F. Zhi-Jie, S. Li-Jie, L. Yong-Hui, First-principle study of native defects in $CuScO_2$ and $CuYO_2$, Chin. Phys. B 17 (2008) 4279–4284.
[32] M. Younsi, S. Saadi, A. Bouguelia, A. Aider, M. Trari, Synthesis and characterization of oxygen-rich delafossite $CuYO_{2+x}$ application to H_2-photo production, Sol. Energy Mater. Sol. Cells 91 (2007) 1102–1109.
[33] Z. Deng, X. Fang, R. Tao, W. Dong, S. Zhou, G. Meng, J. Shao, Effect of Ca-doping on the structural and electrical properties of $CuY_{1-x}Ca_xO_2$ ($0 \le x \le 0.10$) ceramics, J. Alloys Compd. 509 (2011) 5300–5304.
[34] N. Tsuboi, H. Ohara, T. Hoshino, S. Kobayashi, K. Kato, F. Kaneko, Luminescence properties of delafossite-type $CuYO_2$ doped with calcium, oxygen or rare earth Tb, Jpn. J. Appl. Phys. 44 (2005) 765–768.
[35] G. Kresse, J. Furthmuller, Efficiency of ab-initio total energy calculations for metals and semiconductors using a plane-wave basis set, Comput. Mater. Sci. 6 (1996) 15, https://doi.org/10.1016/0927-0256(96)00008-0.
[36] P.E. Blöchl, Projector augmented-wave method, Phys. Rev. B 50 (1994) 17953–17979.
[37] J.P. Perdew, S. Burke, M. Ernzarhof, Generalized gradient approximation made simple, Phys. Rev. Lett. 77 (1996) 3865, https://doi.org/10.1103/PhysRevLett.77.3865.
[38] J. Monkhorst, J. Pack, Special points for brillouin-zone integrations, Phys. Rev. B 13 (12) (1976) 5188–5192, https://doi.org/10.1103/PhysRevB.13.5188.
[39] J. Heyd, G.E. Scuseria, M. Ernzerhof, Hybrid functionals based on a screened coulomb potential, J. Chem. Phys. 118 (2003) 8207–8215.
[40] K. Momma, F. Izumi, *VESTA3* for three-dimensional visualization of crystal, volumetric and morphology data, J. Appl. Crystallogr. 44 (2011) 1272–1276, https://doi.org/10.1107/S0021889811038970.
[41] C. Freysoldt, J. Neugebauer, C.G. Van de Walle, Fully ab initio finite-size corrections for charged-defect supercell calculations, Phys. Rev. Lett. 102 (2009), 016402.
[42] M.H. Naik, M. Jain, Coffee: corrections for formation energy and eigenvalues for charged defect simulations, Comput. Phys. Commun. 226 (2018) 114–126.
[43] B.U. Kathler, M. Jansen, Darstellung und strukturdaten von $CuMO_2$ (M = Al, Ga, Sc, Y), Z. Anorg. Allg. Chem. 543 (1986) 73–80.
[44] T. Ishiguro, N. Ishizawa, N. Mizutani, M. Kato, A new delafossite-type compound $CuYO_2$: I. synthesis and characterization, J. Solid State Chem. 49 (1983) 232–236.
[45] P. Erhart, K. Albe, Modeling the electrical conductivity in $BaTiO_3$ on the basis of first-principles calculations, J. Appl. Phys. 104 (2008) 044315.
[46] C. Cheng, Z.L. Lv, Y. Cheng, G.F. Ji, Structural, elastic and electronic properties of $CuYO_2$ from first-principles study, J. Alloys Compd. 603 (2014) 183–189.
[47] Q.J. Liu, N.C. Zhang, Y.Y. Sun, F.S. Liu, Z.T. Liu, Structural, mechanical, electronic, optical properties and effective masses of $CuMO_2$ (M = Sc, Y, La) compounds: first-principles calculations, Solid State Sci. 31 (2014) 37–45.
[48] M.F. Iozzi, P. Vajeeston, R. Vidya, P. Ravindran, H. Fjellvag, Structural and electronic properties of transparent conducting delafossite: a comparison between the $AgBO_2$ and $CuBO_2$ families (B = Al, Ga, In, Sc and Y), RSC Adv. 5 (2015) 1366–1377.
[49] C. Freysoldt, B. Grabowski, T. Hickel, J. Neugebauer, G. Kresse, A. Janotti, C. G. Van de Walle, First-principles calculations for point defects in solids, Rev. Mod. Phys. 86 (2014) 253–305.

[50] S.B. Zhang, J.E. Northrup, Chemical potential dependence of defect formation energies in gaas: application to ga self-diffusion, Phys. Rev. Lett. 67 (1991) 2339–2342.

[51] F.A. Benko, F.P. Koffyberg, The optical bandgap and band-edge positions of semiconducting p-type $CuYO_2$, Can. J. Phys. 63 (1985) 1306–1308.

[52] T. Ehara, Preparation of $CuYO_2$ thin films by sol-gel method using copper acetate and yttrium acetate as metal sources, J. Chem. Eng. Mater. Sci. 4 (2016) 24–28.

[53] M. Jayaraj, A. Draeseke, J. Tate, A. Sleight, p-type transparent thin films of $CuY_{1-x}Ca_xO_2$, Thin Solid Films 397 (2001) 244–248.

[54] M. Trari, A. Bouguelia, Y. Bessekhouad, p-type $CuYO_2$ as hydrogen photocathode, Sol. Energy Mater. Sol. Cells 90 (2006) 190–202.

[55] M. Gajdos, K. Hummer, G. Kresse, J. Furthmüller, F. Bechstedt, Linear optical properties in the projector-augmented wave methodology, Phys. Rev. B 73 (2006), 045112.